Research Article Vol. 27, No. 1 | 7 Jan 2019 | OPTICS EXPRESS 166

Optics EXPRESS

Experimental quantification of the free-carrier effect in silicon waveguides at extended wavelengths

DAVID E. HAGAN,[1,*] MILOS NEDELJKOVIC,[2] WEI CAO,[2]
DAVID J. THOMSON,[2] GORAN Z. MASHANOVICH,[2] AND
ANDREW P. KNIGHTS[1]

[1] *Department of Engineering Physics, McMaster University, 1280 Main Street West, Hamilton, ON, Canada*
[2] *Optoelectronics Research Centre, University of Southampton, Southampton, SO17 1BJ, UK*
[*] *hagand3@mcmaster.ca*

Abstract: We examine the electro-optic effect at wavelengths ranging from 1.31 to 2.02 μm for: (1) an Electronic Variable Optical Attenuator (EVOA); and (2) a Micro-Ring Resonator (MRR). For the EVOA, simulations were performed to ascertain the relationship between free-carrier concentration and optical attenuation, and are in agreement with our observation of an increase in attenuation with increasing wavelength. MRRs were fabricated for use around wavelengths of 2 μm to explore the sensitivity of operation to bus-to-ring coupling gap and *p*-*n* junction offset. Trends observed in the experiment are replicated by simulation, calibrated using the observations of the EVOA operation. The previously proposed efficiency increase of operation around 2 μm compared to more traditional wavelengths is demonstrated. Future development of devices for these wavelengths, supported by amplification using Thulium Doped Fiber Amplifier (TDFA) technology, is a promising route to aid in the alleviation of increasing demands on communication networks.

1. Introduction

Recent expansion of silicon photonics interest into the mid-infrared (MIR) wavelength region has given rise to developments in sensing [1], nonlinear optics [2], and semiconductor lasers [3]. Telecommunication applications have received specific interest as a result of the looming data bandwidth bottleneck [4] with MIR silicon photonics seen to offer a cost-effective method to manufacture integrated components. The *C*-band, most often used in telecommunication infrastructure, is a wavelength range defined by the amplification spectrum of the Erbium-Doped Fiber Amplifier (EDFA) and the low-loss transmission spectrum of long-haul optical fibers. However, the finite laser and filter linewidth used in Wavelength Division Multiplexing (WDM) systems places a limit on the spectral efficiency of any wavelength band. An attractive solution is to open a parallel window in the MIR wavelength regime defined by the TDFA gain band [5], the MIR equivalent to the EDFA centered around 2 μm. With the advent of the TDFA and advances in hollow core photonic bandgap fibers [6] along with silicon-on-insulator (SOI) high-speed MIR detectors [7], and modulators [8], many components are in place to develop this multi-band telecommunications infrastructure.

An important device in various photonic systems is the variable optical attenuator (VOA) [9] which allows for precise control over the intensity of light through a system. This is particularly important for devices which can exhibit detrimental nonlinearities at high-power such as the observation of self-heating in micro-ring resonators (MRR) [10, 11]. The silicon-based carrier injection EVOA makes use of the electro-optic effect; the well-studied perturbation of a material's complex refractive index by means of free-carrier interaction [12]. Such free-carriers can be introduced intentionally via *p*-*n* structures formed through CMOS-compatible dopant implantation processes and may be used for optical modulation. As the strength of the free-carrier effect is

#345993 https://doi.org/10.1364/OE.27.000166
Journal © 2019 Received 18 Sep 2018; revised 11 Dec 2018; accepted 12 Dec 2018; published 3 Jan 2019

approximately proportional to the square of wavelength, devices based on the free-carrier effect can be designed for longer wavelengths (compared to the traditional communication bands) with a reduced device footprint and/or lower power consumption.

Devices operating around a wavelength of 2 μm have gained significant attention due to the recent availability of the TDFA, and the promise of TDFA-band communication systems. Of particular interest as a high-speed modulator is the MRR which boasts a large "on-off" extinction ratio and low energy consumption; less than 50 fJ/bit under reverse-bias [13]. In a recently submitted paper [14] we demonstrated modulation using an MRR operating at 2 μm, however, to our knowledge, no systematic study of MRR modulator operation to design parameter variation has yet been performed.

In this paper, we study the electro-optic effect strength in silicon at a 2 μm wavelength in a forward-bias EVOA and demonstrate the steady-state operation of a MRR modulator. Both sets of experimental data are modeled using an empirical expression for the plasma dispersion effect in silicon. The simulations are such that there exists self-consistency.

2. Methods and experimental set-up

Active devices in silicon photonics make use of implanted dopants as a means of electrical connection as well as optical phase and amplitude modulation in waveguides (the so-called free-carrier effect) [12], whereby a material with excess electrons or holes experiences a wavelength dependent change in complex refractive index. By changing the concentration of free-carriers in a silicon waveguide, the phase and amplitude of the propagating mode can therefore be modulated. This is the operating principle behind phase modulation devices such as the Mach-Zehnder and MRR modulator, as well as amplitude modulating devices such as the EVOA.

Changes in the real index Δn and the absorption $\Delta\alpha$ in silicon due to free-carriers can be approximated using the Drude model [12] such that:

$$\Delta n = -\left(\frac{e^2\lambda^2}{8\pi^2c^2\varepsilon_0 n}\right)\left[\frac{\Delta N_e}{m_{ce}^{*2}} + \frac{\Delta N_h}{m_{ch}^{*2}}\right], \tag{1}$$

$$\Delta\alpha = \left(\frac{e^3\lambda^2}{4\pi^2c^3\varepsilon_0 n}\right)\left[\frac{\Delta N_e}{m_{ce}^{*2}} + \frac{\Delta N_h}{m_{ch}^{*2}}\right], \tag{2}$$

where e is the charge of an electron, λ is the wavelength, c is the speed of light, ε_0 is the permittivity of free space, n is the unperturbed refractive index of silicon, ΔN_e and ΔN_h are the changes in electron and hole concentrations in silicon, m_{ce}^* and m_{ch}^* are the conductivity effective masses of electrons and holes, and μ_e and μ_h are the electron and hole mobilities respectively. The Drude model provides an excellent approximation to plasma dispersion in silicon but has been found to deviate from experimental data [12]. An empirical model has been developed [15] motivated by limitations of the Drude model, especially at extended wavelengths. This model employs a Kramers-Kronig analysis of experimentally measured absorption spectra to estimate free-carrier refraction and absorption for wavelengths from 1.31 to 14 μm in silicon, resulting in simple wavelength-specific equations for Δn and $\Delta\alpha$ which vary only with ΔN_e and ΔN_h. These equations for a wavelength of 2 μm are:

$$\Delta\alpha = 3.22x10^{-20}\Delta N_e^{1.149} + 6.21x10^{-20}\Delta N_h^{1.119}, \tag{3}$$

$$-\Delta n = 1.91x10^{-21}\Delta N_e^{0.992} + 2.28x10^{-18}\Delta N_h^{0.841} \tag{4}$$

Recently [16] it was used to simulate dopant induced loss in submicron waveguides showing very good agreement with measured results. We apply this empirical model to simulate optical attenuation in a commercial EVOA and modulation using MRRs.

2.1. EVOA

To explore free-carrier absorption as a function of wavelength we employed an EVOA operating at wavelengths ranging from 1.31 to 2.02 μm. The device is a relatively large cross-section single-mode silicon waveguide (3 μm wide, 4.2 μm high with a 2.8 μm slab thickness) with an integrated *p-i-n* diode operating under carrier injection controlled via external bias. The *p* and *n* doping are positioned more than 4 μm from the waveguide edge to prevent measurable parasitic optical absorption when the diode is unbiased. The fabrication details and geometrical description of the device are provided in [17].

The laser sources used for measurements at 1.31, 1.51-1.64, and 2.02 μm were a Luminent MRLDSP04OP laser diode, Agilent 81640A tuneable laser source, and an Eblana Photonics 2020-FP series laser diode, respectively. Similarly the EVOA output light was coupled into an ILX Lightwave FPM-8200 power meter, Agilent 81635A power sensor, and a Thorlabs PDA10D InGaAs detector, respectively. The fiber coupled laser sources were launched into the EVOA via an integrated mode converter that provided efficient coupling at all wavelengths. The EVOA was placed under forward bias using a Keithley 2400 source meter and electrical probes.

2.2. MRR

Phase modulation is exploited in devices such as the MRR modulator, the operation of which has been studied extensively [18]. The resonant wavelength of an MRR is given by:

$$\lambda_{res} = \frac{n_{eff}L}{m}, \quad m = 1, 2, 3, \ldots \tag{5}$$

where n_{eff} is the effective index of the propagating mode and L is the cavity length. Examining Eq. (1), it can be seen that under carrier-injection, ΔN_e and ΔN_h increase causing the effective index of the mode to decrease resulting in a blue-shift of the resonant wavelength of the MRR. Under carrier-depletion, the opposite results in a red-shift in the resonant wavelength.

MRR modulators in an add-drop configuration were designed and fabricated via CMC Microsystems through A*STAR IME on a 220 nm SOI platform with a waveguide width of 600 nm, slab height of 90 nm, and a ring radius of 10 μm. A device schematic layout and cross-section can be seen in Fig. 1.

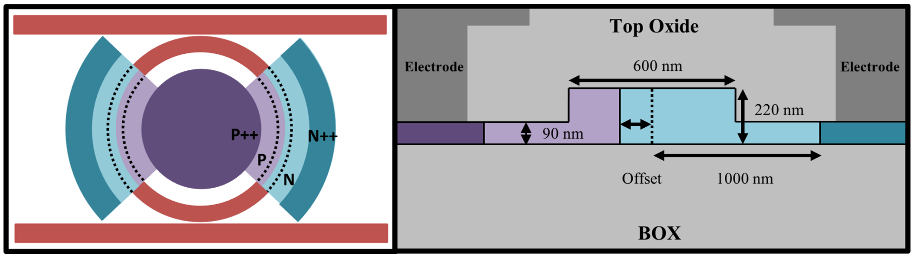

Fig. 1. MRR modulator schematic layout (left) and phase-shifter cross-section (right).

The active region covers 64% of the total ring circumference. The inner and outer-ring portion of the waveguide is *p*-and *n*-doped, respectively, with doping concentrations of $4.8\text{x}10^{17}$ and $2.8\text{x}10^{17}$ cm^{-3} which were determined previously [16]. The *p-n* junction offset was varied to optimize resonance shift efficiency.

The MRR was subjected to linearly polarized light from a Sacher Lasertechnik tuneable Littman/Metcalf laser coupled into the bus waveguide via a 180 nm wide inverse nanotaper. The output was coupled via an identical nanotaper into a tapered fiber and then into a Thorlabs PDA10D InGaAs detector. A Keithley 2400 source meter and DC electrical probes were used to electrically bias the MRR.

3. Results and discussion

Attenuation measurements via the EVOA were performed for each wavelength as a function of applied forward bias. We estimate the coupling loss to be less than 5 dB per facet for 1550 nm confirming the relatively good optical coupling of the silicon taper used for these devices. The optical output power under zero-bias was used to normalize the biased optical output attenuated by the EVOA shown in Fig. 2, such that a relative comparison between wavelengths could be made. We note that with increasing current, the attenuation increases until the injection of free-carriers saturates.

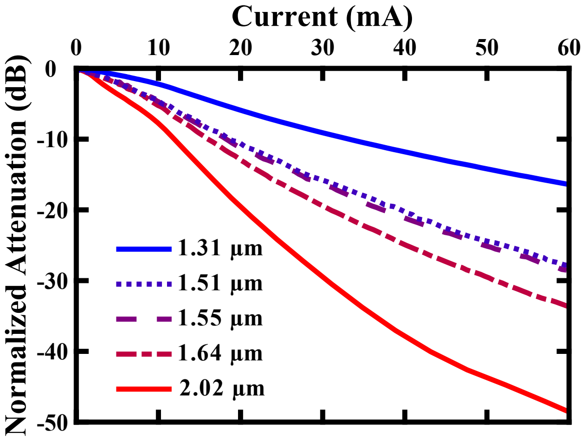

Fig. 2. Normalized EVOA optical attenuation under forward bias for a range of input wavelengths.

An increase in attenuation efficiency is seen as the wavelength is varied from 1.31 to 2.02 μm confirming the expected increase in free-carrier absorption at longer wavelengths due to the increasing cross-section for photon/free-carrier interaction. This wavelength dependency is evident in Fig. 3 which shows the measured optical attenuation (normalized to the zero bias output for each wavelength) as a function of wavelength plotted for several lines of constant injection current.

The attenuation in dB (relative to the unbiased condition) is essentially linear as a function of wavelength across this wavelength range. From Eq. (2), we expect the change in absorption at 2 μm to be approximately 1.7 times greater than at 1.55 μm as predicted by [15].

The cross-sectional dimensions of the device (determined by focused ion beam analysis) were used in a model utilizing finite-element method simulation to generate the mode profile for all wavelengths experimentally measured. The optical confinement coefficient (Γ, defined as the fraction of mode energy density residing in the waveguide core) for all wavelengths was calculated to be almost invariant at $\Gamma = 0.92$ and $\Gamma = 0.91$ for the fundamental TE and TM modes, respectively. The aforementioned empirical model for free-carrier absorption [15] was used to calculate the complex refractive index of the waveguide under forward bias. Under equilibrium conditions, the concentration of electrons and holes is assumed to be equal, although the optical absorption due to holes is greater than that for electrons. The simulated absorption for 1.31, 1.55, and 2.02 μm is shown in Fig. 4.

The normalized attenuation dependencies were derived by choosing the simulated material absorption coefficient according to [15] for both electrons and holes. The measured attenuation for each driving current is shown in Fig. 4 as three vertical sets of solid markers. To estimate the steady-state electron and hole concentrations present in the VOA, these measured data sets

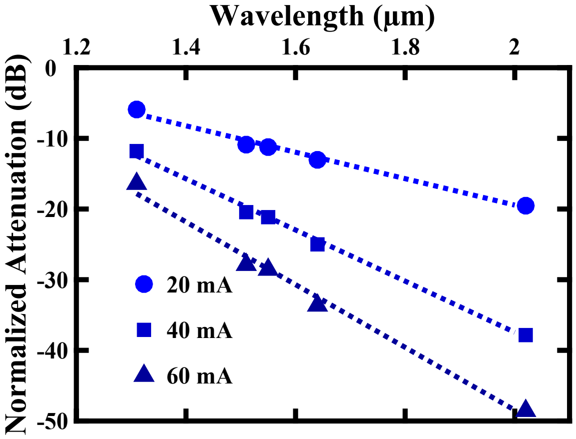

Fig. 3. Normalized attenuation isocurrent lines as a function of wavelength. Dotted lines represent a linear regression of measured data.

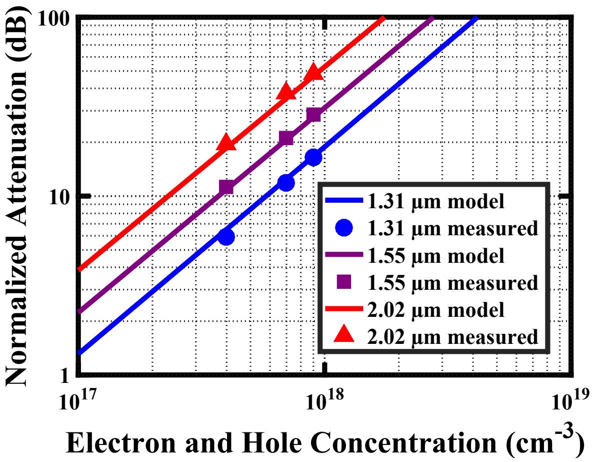

Fig. 4. Simulated free-carrier absorption in the VOA as a function of carrier concentration. Measured data at fixed driving currents are also plotted.

are fitted such that they provide the best overall match between the solid lines which result from the modeling described above. The resulting steady-state electron-hole concentration for 20, 40, and 60 mA of driving current are 4x10^{17}, 7x10^{17}, and 9x10^{17} cm^{-3}, respectively, and appear reasonable for a *p-i-n* silicon diode of this nature [19]. Further, these free-carrier concentrations are consistent with a silicon EVOA with these cross-sectional dimensions and driving currents [9, 20].

For EVOA designs with sub-micron cross-section waveguides, operation at relatively high-speed is possible [21]. Although not explored further in this work, we note that for wavelengths around 2 μm, attenuation-based modulation may be achieved at lower power or with reduced footprint than at more common communication wavelengths such as those in the *O*, *C* and *L* bands.

The MRR optical transfer spectrum for biases from -10 to 1 V is shown in Fig. 5 (left). The extracted resonance shift (with respect to zero bias) is plotted in Fig. 5 (right). The MRR under

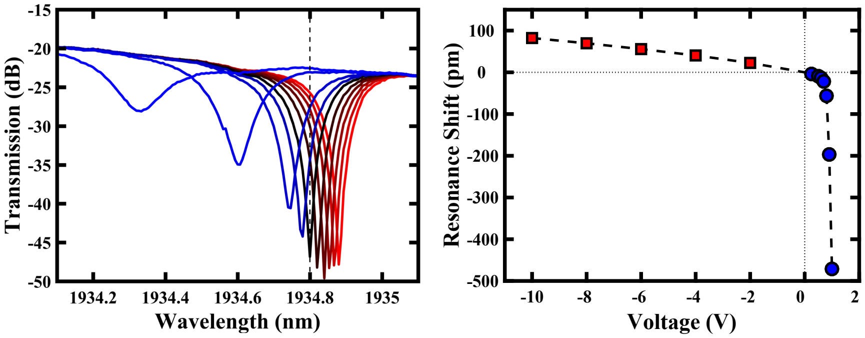

Fig. 5. Measured MRR spectrum for biases from -10 to 1 V (left) and extracted resonance shift (right). The dashed lines denote zero bias resonance positions.

forward bias of 1 V exhibits a relatively large blue-shift of 471 pm; a result of the large number of injected carriers in this operational regime. This result is consistent with both a substantial decrease in MRR *Q*-factor from 10,000 to 7,500 (calculated as the ratio of resonant wavelength to FWHM), and a decrease in filter notch depth from 24 to 7 dB.

Carrier depletion in a reverse-bias MRR has been studied theoretically in [22]. An approach to simulate the resonance shift in a MRR modulator begins with solving for the MRR waveguide mode analytically using the effective index method described in [23]. Next, a 1-D free-carrier concentration profile is calculated for zero and reverse biases using simple analytical expressions for an abrupt *p*-*n* junction with user-defined dopant concentrations and junction offset [19], which in our case determined concentrations of 2.8x10^{17} and 4.8x10^{17} cm^{-3} for the *p*- and *n*-doped regions respectively. The electron and hole distributions are used to calculate the voltage-dependent change in effective index through an overlap integral of the solved mode profile with the free-carrier profile. In predicting the index perturbation caused by the free-carriers, the model for plasma dispersion in [22] is modified using the model described in reference [15]. This is justified by the consistency of simulated and measured results from the EVOA experiment. Finally, the change in effective index for each voltage is used to determine the resonance shift of the MRR analytically from reference [18].

The measured and simulated results for a device with 30 nm *p*-*n* junction offset from the waveguide center are shown in Fig. 6. The measured resonance shift versus reverse bias for a wavelength of 1.97 μm is in reasonable agreement with the simulated results, albeit the simulations provide a greater shift. In comparison, simulations of identically doped MRRs operating at 1.97 μm and 1.55 μm wavelengths with waveguide widths of 600 and 450 nm, respectively, show enhanced modulation efficiency in the former due to the stronger free-carrier effect at the longer wavelengths.

Resonance shift measurements were performed for *p*-*n* junction offsets varying from 0 to 240 nm and compared with simulation. These results are shown in Fig. 7. Experimentally measured results demonstrate reasonable agreement with simulation (at least in terms of the data trend) and show an optimal junction offset of approximately 30 nm for these doping concentrations. Deviation from measured and simulated results in Fig. 6 and Fig. 7 may be attributed to several factors but perhaps dominant is the use of a 1-D *p*-*n* junction approximation, coupled with the effective index method [23], for solving the overlap between the propagating mode and the free-carrier profiles. Additionally, any variation in the waveguide mode in the ring compared to that in a straight waveguide is unaccounted for in the simulation. This effect can shift the modal power distribution in the waveguide and thus the optimal *p*-*n* junction offset value [24].

The highly-doped *p*++ and *n*++ regions in the MRR used to provide low resistance contact to

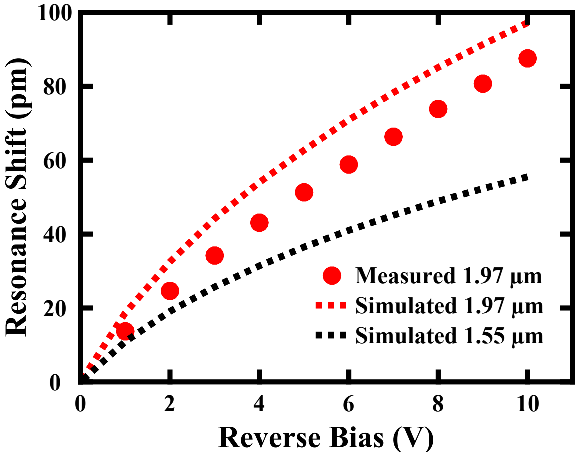

Fig. 6. Measured and simulated reverse-bias resonance shift for a MRR modulator with a 30 nm *p-n* junction offset. Dashed black line indicates simulation of a 1.55 μm MRR modulator with 450 nm waveguide width.

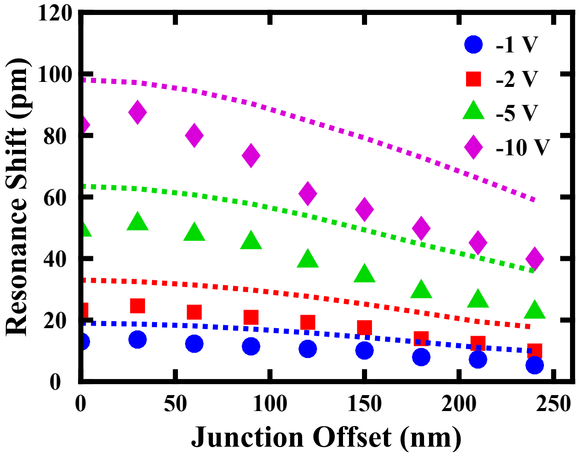

Fig. 7. Measured and simulated reverse-bias resonance shift for varying *p-n* junction offset. Dashed line denotes simulated results

the *p-n* junction are separated from the waveguide edges by a distance of 1 μm. The separation presents a trade-off between parasitic loss from mode overlap, and increasing electrical bandwidth from reduced device resistance. For high-speed modulation, this separation is a crucial parameter in determining the extinction ratio and electrical bandwidth [25]. The choice in waveguide width and *p-n* junction doping concentrations also present trade-offs between modulation efficiency and electrical bandwidth. The waveguide width of 600 nm was chosen here such that the waveguide is below the single-mode cut-off point. Although increasing waveguide width and thus confinement can increase reverse-bias modulation efficiency, beyond a critical width the total optical power overlapping the *p-n* junction depletion width begins to decrease significantly. Similarly, increasing the *p-n* junction doping concentrations reduces the junction resistance and thus can increase the electrical bandwidth, but at the expense of reduced depletion region growth under reverse-bias. The inclusion of an add-drop bus waveguide is done to reduce the photon lifetime that future high-speed modulation measurements may be limited by. Longer wavelengths exhibit lower intrinsic propagation loss due to scattering in single-mode waveguides, thus for a reverse-bias MRR modulator operating at longer wavelengths, the photon lifetime can be a limiting factor in modulation bandwidth due to the low cavity loss, though this can be partially offset by the increased loss from free-carriers.

High-speed operation of a MRR is contingent on the RC-time constant of the active region as well as the photon lifetime in the ring which is proportional to the Q-factor. The photon lifetime-limited bandwidth is given by [26]:

$$f_0 = \frac{c}{Q\lambda} = \frac{c\alpha}{\pi n_g}, \tag{6}$$

where c is the speed of light, Q is the Q-factor of the resonance, and λ is the wavelength. The equation encompasses the waveguide's group index n_g and loss coefficient α. In comparing all-pass configuration MRRs designed for 1.97 and 1.55 μm described in Fig. 6, the former has a lower group index and higher loss due to free-carriers for identical p-n junctions implying a larger photon lifetime-limited bandwidth. The addition of an add-drop waveguide, as done in this work, further increases this bandwidth limit by reducing the Q-factor in a controllable manner. For the data presented, the estimated photon lifetime-limited bandwidth is 15 GHz at 0 V and 20 GHz at 1 V. The electrical RC-limited bandwidth will be examined in future work but is expected to be lower than that of 1550 nm optimized MRR devices due to the increased waveguide width and separation of highly doped p++ and n++ regions. Further work will explore the high-speed operation of MRR modulators and in particular the impact of the relative increase of the electro-optic coefficient with increasing wavelength.

4. Conclusion

This work details experimental evidence of the impact of increasing wavelength on the operation of silicon photonic devices employing the free-carrier plasma-dispersion effect. Measured results verify enhanced optical attenuation at longer wavelengths using a silicon EVOA. Change in free-carrier absorption is shown to be approximately 1.7 times greater for 2.02 μm compared to 1.55 μm. Optical modulation of TDFA-band wavelengths using a MRR modulator is demonstrated, and the results are simulated using an analytical model. An increase in modulator efficiency, in terms of resonance shift in simulated optimized structures, is again shown to be approximately 1.7 times greater for 1.96 μm relative to 1.55 μm. These results imply free-carrier based devices with lower operating power and smaller footprint can be used in future TDFA compatible wavelength telecommunication architectures employing silicon photonics. In addition, the results support the empirical free-carrier model of [15], which can be used with confidence in future device design.

References

1. R. Soref, "Mid-infrared photonics in silicon and germanium," Nat. Photonics **4**, 495–497 (2010).
2. S. Zlatanovic, J. S. Park, S. Moro, J. M. C. Boggio, I. B. Divliansky, N. Alic, S. Mookherjea, and S. Radic, "Mid-infrared wavelength conversion in silicon waveguides using ultracompact telecom-band-derived pump source," Nat. Photonics **4**, 561–564 (2010).
3. B. Jalali, V. Raghunathan, R. Shori, S. Fathpour, D. Dimitropoulos, and O. Stafsudd, "Prospects for Silicon Mid-IR Raman Lasers," IEEE J. Sel. Top. Quantum Electron. **12** (2006).
4. R. Won, "View from... Communication Networks Beyond the Capacity Crunch: Is it crunch time?" Nat. Photonics **9**, 424–426 (2015).
5. Z. Li, A. M. Heidt, N. Simakov, Y. Jung, J. M. O. Daniel, S. U. Alam, and D. J. Richardson, "Diode-pumped wideband thulium-doped fiber amplifiers for optical communications in the 1800 - 2050 nm window." Opt. Express **21**, 26450–5 (2013).
6. Y. Chen, Z. Liu, S. R. Sandoghchi, G. T. Jasion, T. D. Bradley, E. Numkam Fokoua, J. R. Hayes, N. V. Wheeler, D. R. Gray, B. J. Mangan, R. Slavík, S. Member, F. Poletti, M. N. Petrovich, D. J. Richardson, Y. Chen, Z. Liu, S. R. Sandoghchi, G. T. Jasion, T. D. Bradley, E. Numkam, J. R. Hayes, N. V. Wheeler, D. R. Gray, R. Slavík, F. Poletti,

M. N. Petrovich, and D. J. Richardson, “Multi-kilometer Long, Longitudinally Uniform Hollow Core Photonic Bandgap Fibers for Broadband Low Latency Data Transmission,” J. Light. Technol. **34** (2016).

7. J. J. Ackert, D. J. Thomson, L. Shen, A. C. Peacock, P. E. Jessop, G. T. Reed, G. Z. Mashanovich, and A. P. Knights, “High-speed detection at two micrometres with monolithic silicon photodiodes,” Nat. Photonics **9**, 393–396 (2015).
8. M. A. Van Camp, S. Assefa, D. M. Gill, T. Barwicz, S. M. Shank, P. M. Rice, T. Topuria, and W. M. J. Green, “Demonstration of electrooptic modulation at 2165nm using a silicon Mach-Zehnder interferometer,” Opt. Express **20**, 28009–16 (2012).
9. D. J. Thomson, L. Shen, J. J. Ackert, E. Huante-Ceron, A. P. Knights, M. Nedeljkovic, A. C. Peacock, and G. Z. Mashanovich, “Optical detection and modulation at 2μm-2.5μm in silicon,” Opt. Express **22**, 10825 (2014).
10. T. Xiaogang, L. Jun, and X. Chenyang, “Thermal nonlinear effect in high Q factor silicon-on-insulator microring resonator,” Opt. Commun. **395**, 207–211 (2017).
11. Z. Zhang, G. I. Ng, H. Qiu, W. Wang, X. Guo, M. S. Rouifed, C. Liu, and H. Wang, “Compact microring resonators integrated with grating couplers working at 2 μm wavelength on silicon-on-insulator platform,” Appl. Opt. **56**, 5444 (2017).
12. R. A. Soref and B. R. Bennett, “Electrooptical effects in silicon,” IEEE J. Quantum Electron. **23**, 123–129 (1987).
13. P. Dong, S. Liao, D. Feng, H. Liang, D. Zheng, R. Shafiiha, C.-C. Kung, W. Qian, G. Li, X. Zheng, A. V. Krishnamoorthy, and M. Asghari, “Low V_pp, ultralow-energy, compact, high-speed silicon electro-optic modulator,” Opt. Express **17**, 22484 (2009).
14. W. Cao, D. E. Hagan, D. J. Thomson, M. Nedeljkovic, C. G. Littlejohns, A. P. Knights, S.-U. Alam, J. Wang, F. Gardes, M.-S. Rouifed, T. G. Xin, W. Wang, H. Wang, G. T. Reed, and G. Z. Mashanovich, “High speed modulators in silicon-on-insulator for the 2 μm wavelength band,” Optica (to be published).
15. M. Nedeljkovic, R. Soref, and G. Z. Mashanovich, “Free-carrier electrorefraction and electroabsorption modulation predictions for silicon over the 1-14-μm infrared wavelength range,” IEEE Photonics J. **3**, 1171–1180 (2011).
16. D. E. Hagan and A. P. Knights, “Mechanisms for optical loss in SOI waveguides for mid-infrared wavelengths around 2 μm,” J. Opt. **19**, 025801 (2017).
17. A. Martin, D. Feng, J. Luff, and M. Asghari, “Technical Challenges for Silicon Photonics Transceivers for Data Center Applications,” in *Optical Fiber Communication Conference,* (Optical Society of America, 2016).
18. W. Bogaerts, P. De Heyn, T. Van Vaerenbergh, K. De Vos, S. Kumar Selvaraja, T. Claes, P. Dumon, P. Bienstman, D. Van Thourhout, and R. Baets, “Silicon microring resonators,” Laser & Photonics Rev. **6**, 47–73 (2012).
19. S. M. Sze and K. K. Ng, *Physics of semiconductor devices* (Wiley-Interscience, 2007).
20. D. W. Zheng, B. T. Smith, and M. Asghari, “Improved efficiency Si-photonic attenuator,” Opt. Express **16**, 16754 (2008).
21. J. Xia, J. Yu, Q. Yan, and Z. Liu, “High-speed electrooptical VOA integrated in silicon-on-insulator,” Chin. Opt. Lett. **1**, 217–219 (2003).
22. L. Chrostowski and M. Hochberg, *Silicon Photonics Design: from devices to systems* (Cambridge University, Cambridge, 2015).
23. D. L. Lee, *Electromagnetic principles of integrated optics* (John Wiley & Sons Inc, 1986).
24. A. Brimont, X. Hu, S. Cueff, P. Rojo Romeo, G. Saint Girons, A. Griol, A. Zanzi, P. Sanchis, and R. Orobtchouk, “Low-Loss and Compact Silicon Rib Waveguide Bends,” IEEE Photonics Technol. Lett. **28**, 299–302 (2016).
25. S. S. Azadeh, F. Merget, S. Romero-García, A. Moscoso-Mártir, N. von den Driesch, J. Müller, S. Mantl, D. Buca, and J. Witzens, “Low V_π Silicon photonics modulators with highly linear epitaxially grown phase shifters,” Opt. Express **23**, 23526 (2015).
26. G. Li, X. Zheng, J. Yao, H. Thacker, I. Shubin, Y. Luo, K. Raj, J. E. Cunningham, and A. V. Krishnamoorthy, “25Gb/s 1V-driving CMOS ring modulator with integrated thermal tuning,” Opt. Express **19**, 20435 (2011).